

ON THE DISCREPANCY BETWEEN THEORETICAL AND X-RAY CONCENTRATION–MASS RELATIONS FOR GALAXY CLUSTERS

E. RASIA¹, S. BORGANI^{2,3,4}, S. ETTORI^{5,6}, P. MAZZOTTA^{7,8}, AND M. MENEGHETTI^{5,6}

¹ Department of Physics, University of Michigan, 450 Church Street, Ann Arbor, MI 48109, USA

² Dipartimento di Fisica dell' Università di Trieste, Sezione di Astronomia, via Tiepolo 11, I-34131 Trieste, Italy

³ INAF, Osservatorio Astronomico di Trieste, via Tiepolo 11, I-34131, Trieste, Italy

⁴ INFN, Istituto Nazionale di Fisica Nucleare, Trieste, Italy

⁵ INAF, Osservatorio Astronomico di Bologna, via Ranzani 1, I-40127, Bologna, Italy

⁶ INFN, Sezione di Bologna, viale Berti Pichat 6/2, I-40127, Bologna, Italy

⁷ Dipartimento di Fisica, Università di Roma Tor Vergata, via della Ricerca Scientifica, I-00133, Roma, Italy

⁸ Harvard-Smithsonian Center for Astrophysics, 60 Garden Street, Cambridge, MA 02138, USA

Draft version June 15, 2021

ABSTRACT

In the past 15 years, the concentration–mass relation has been investigated diffusely in theoretical studies. On the other hand, only recently has this relation been derived from X-ray observations. When that happened, the results caused a certain level of concern: the X-ray normalizations and slopes were found significantly dissimilar from those predicted by theory.

We analyzed 52 galaxy clusters and groups, simulated with different descriptions of the physical processes that affect the baryonic component, with the purpose of determining whether these discrepancies are real or induced by biases in the computation of the concentration parameter or in the determination of the selection function of the cluster sample for which the analysis is carried out. In particular, we investigate how the simulated concentration–mass relation depends (1) on the radial range used to derive the concentration, (2) on the presence of baryons in the simulations, and on the effect of star formation and feedback from supernovae and active galactic nuclei (AGNs). Finally, we evaluate (3) how the results differ when adopting an X-ray approach for the analysis and (4) how the selection function based on X-ray luminosity can impact the results. All effects studied go in the direction of alleviating the discrepancy between observations and simulations, although with different significance: while the choice of the radial range to fit the profiles and the inclusion of the baryonic component play only a minor role, the X-ray approach to reconstruct the mass profiles and the selection of the cluster sample have a strong impact on the resulting concentration–mass relation.

Extending the fit to the most central regions or reducing the fitting radius from the virial boundary to the typical X-ray external radius causes an increase of the normalization in radiative simulations by 5%-10%. In the second case, we measure a slope that is up to twice steeper than that derived by using the typical theoretical radial range. Radiative simulations including only supernova feedback produce 30% higher concentrations than the dark matter case. Such a difference is largely reduced when including the effect of AGN feedback. The concentration–mass relation derived from the X-ray synthetic catalog is significantly steeper due to the combination of several different effects, such as environment, dynamical state and dynamical history of the clusters, bias in mass and temperature measurements, and their dependence on the radius and on the mass of the system. Finally, selecting clusters according to their X-ray luminosity produces a net increase in both normalization and slope of the relation, since at fixed mass, the most luminous clusters are also the most concentrated.

Subject headings: cosmology: theory – galaxies: clusters: general – galaxies: clusters: intracluster medium – methods: numerical – X-ray: galaxies: clusters

1. INTRODUCTION

The dark sector (dark energy and dark matter (DM)) exceeds by about 25 times the baryonic content of our universe (e.g. Voit 2005; Borgani & Kravtsov 2011; Allen et al. 2011 for recent reviews on cosmology with focus on galaxy clusters). As a consequence, at first approximation, we may assume that simulations with only dark components properly describe the salient halo properties such as the mass distribution, the tridimensional halo shape, the density profile, and the concentration (see Kravtsov & Borgani 2012, for a galaxy-cluster-formation review). However, an increasing number of theoretical papers have begun to contest this simplistic view, showing that baryons (in the form of both hot gas and stars) can significantly influence all these topics (e.g. Rudd et al. 2008; Stanek et al. 2009; Duffy et al. 2010; Lau et al. 2011; Gnedin et al. 2011; van Daalen et al. 2011; Cui et al. 2012; Zhu & Pan 2012; Macciò et al. 2012; Governato et al. 2012; Balaguera-Antolínez

& Porciani 2013, among the most recent publications on the various aspects). A certain disagreement between some observational results and theoretical predictions based on DM-only simulations support this discomfort. In this respect, a recent debate about the X-ray observed and simulated concentration–mass ($c-M$) relation warmed up (Fedeli 2012, and references therein). Indeed, while earlier works based on 10-12 clusters observed by *Chandra* (Vikhlinin et al. 2006) and *XMM-Newton* (Pratt & Arnaud 2005; Pointecouteau et al. 2005) showed consistency with theoretical works (Dolag et al. 2004), lately, with the enlargement of the observational collections, more differences have arisen. The $c-M$ relation from the larger X-ray samples of Buote et al. (2007, hereafter B07), Schmidt & Allen (2007, hereafter SA07), and Ettori et al. (2010, hereafter E10) is significantly steeper (Fedeli 2012) than the relation derived from the Millennium simulation (Gao et al. 2008, with results similar to the aforementioned work by Dolag et al. 2004).

An exception to this mismatch is the result by Host & Hansen (2011), who, however, analyzed only 11 systems.

All these works consistently adopt the Navarro–Frenk–White (NFW) analytic model to fit the density profile and derive the concentration. Navarro et al. (1996) showed the existence of a universal profile that well describes the halo density and mass distribution for a large range of halo mass and cosmologies (Navarro et al. 1997). Their fitting formulae are characterized by two parameters: the normalization, ρ_s , and the scale radius, r_s . The expressions for the profiles of the NFW density and the NFW mass, as a function of $x = r/r_s$, are respectively

$$\rho(x) = \frac{\rho_s}{x(1+x)^2}, \quad (1)$$

$$M(<x) = 4\pi\rho_s r_s^3 f_x, \quad f_x = \ln(1+x) - x/(1+x). \quad (2)$$

The logarithmic slope of the density profile measured at the scale radius is equal to -2 , transitioning from the central asymptotic value of -1 to the external value of -3 . The normalization factor is connected to the characteristic over-density, Δ , and to the critical density at the halo redshift z , ρ_{cr} , through

$$\rho_s = \frac{\Delta\rho_{\text{cr}}}{3} \frac{c^3}{\ln(1+c) - c/(1+c)} \quad (3)$$

where the critical density can be expressed as $\rho_{\text{cr}} = 3H^2(z)/(8G)$, with $H(z)$ the Hubble parameter at redshift z and G Newton’s gravitational constant. Finally, c is the concentration of the halo and is defined as the number of times the scale radius is contained within a fixed over-density radius: $c = R_\Delta/r_s$. In the following, we will always define the concentration in relation to the over-density $\Delta = 200$.¹

The origins of the density shape mostly reside on the density and triaxiality of the original peak and on the continuous contraction of the innermost material due to subsequent accretion during the collapse (Dalal et al. 2010). This last point is also a suitable explanation for the increase of the concentration parameter with the decrease of mass (e.g., NFW, Eke et al. 2001; Bullock et al. 2001; Dolag et al. 2004; Zhao et al. 2009). The physical and cosmological justification is linked to the hierarchical scenario of structure formation: small halos form at earlier time when the universe was denser than today and, over time, the sedimentation of material at the center happens in an already-established high-density peak.

Measures of a negative slope from observations are, therefore, expected. The surprise is related to the values: the X-ray slope is up to five times steeper than what is found in DM cosmological simulations. The question we want to answer in this paper is *whether the differences between theory and observations are real* (i.e., some fundamental physical ingredients are missing in theoretical models) *or artificial* (i.e., the comparison is performed without properly accounting for the presence of biases induced by the specific method to select the sample or to measure the concentration). Indeed, it is unquestionable that the basic procedural assumptions of the two analyses differ in several aspects. The *simulated concentration–mass relation* is mostly derived by fitting the NFW profile to the three-dimensional density distribution extracted considering the influence of all the particles without exclusion of sub-structures or sub-clumps, and from the really central region to the outskirts of the halo, usually up to the virial region. The sample

selection is typically volume-limited with a well-defined cut in mass. Finally, as said above, many theoretical works are based on large cosmological boxes of DM only (e.g., Bhattacharya et al. 2013; Kwan et al. 2012, among the most recent ones). On the contrary, the *X-ray concentration–mass relation* is derived from projected data that have a limited radial range because of the signal-to-noise ratio and the field of view. Few clusters have been observed to R_{500} with enough photon statistics and even fewer at R_{200} . For example, E10 (one of the samples we are comparing to) reaches on average 40% of R_{200} (see Section 3.3.1). The observational selection function is not done in mass. In the best case, it depends on the X-ray luminosity. In the worst (and the most common) situation, the clusters are chosen among the ones available in the archives without a well-defined selection function. As a final note, the real universe has baryons.

The possibility that baryons might influence the structure-formation process and, in particular, the DM distribution was introduced almost three decades ago with the development of the analytic model of ‘adiabatic contraction’ (Barnes & White 1984; Blumenthal et al. 1986; Ryden & Gunn 1987). More recently, cosmological simulations push further the improvement of the model (e.g. Gnedin et al. 2004, 2011; Gustafsson et al. 2006; Abadi et al. 2010; Tissera et al. 2010; Zemp et al. 2012; Giocoli et al. 2012). The underlying idea is that, at the center, the DM feels the growth of the total potential well due to the extra baryonic material accreted as a consequence of cooling and condensation. However, even if a specific great effort has been devoted to studying the concentration parameter in non-radiative simulations (e.g. Rasia et al. 2004; Pedrosa et al. 2009; Tissera et al. 2010) only recently have these investigations been extended to include various models of the intra cluster medium (ICM; Rudd et al. 2008; Duffy et al. 2010; Meneghetti et al. 2010; Macciò et al. 2012; Governato et al. 2012; Martizzi et al. 2012; Ragone-Figueroa et al. 2012) and also different dark-energy models (Grossi & Springel 2009; Baldi 2012; De Boni et al. 2013). As for the analysis of hydrodynamical simulations, particular attention has been devoted so far to galaxies and galaxy groups to understand whether the inclusion of baryons can explain the observational presence of cores in the density profiles (e.g. Ogiya & Mori 2011; Macciò et al. 2012; Martizzi et al. 2012; Teyssier et al. 2013). On the contrary, in this work, we will focus on *massive clusters* that cover the same mass range sampled by the X-ray observations analyzed in SA07 and E10.

This paper is organized as follows: after presenting the simulations in Section 2, we discuss the results derived from the intrinsic analysis of the simulated clusters in Section 3. The observational approach applied to synthetic X-ray images will be presented in Section 4, while in Section 5 we will focus on the selection function. Our conclusions are outlined in Section 6.

2. SIMULATIONS

In this section, we briefly describe the four sets of simulated clusters that are used in our intrinsic analysis (Section 3). These four sets are obtained starting from the same initial conditions and using four different physical descriptions of the processes determining the evolution of the baryonic component. More details on the generation of the initial conditions are provided by Bonafede et al. (2011), while we refer to Killedar et al. (2012) for a description of the different physical models implemented,

¹ R_{200} is, therefore, the radius of the sphere enclosing a mean density 200 times the critical density. Conversions of the NFW mass defined for different values of Δ are provided in the Appendix of Hu & Kravtsov (2003) and Appendix of Ettori et al. (2010).

and to Rasia et al. (2012, hereafter R12) for the characterization of the synthetic X-ray catalog.

2.1. The Sets of Simulated Clusters

Our simulated clusters have been chosen within 29 Lagrangian regions identified within a $1 h^{-3} \text{Gpc}^3$ low-resolution N -body cosmological simulation.² The cosmological model assumed is a flat Λ CDM model, with $\Omega_m = 0.24$ for the matter density parameter, $\Omega_{\text{bar}} = 0.04$ for the contribution of baryons, $H_0 = 72 \text{ km s}^{-1} \text{ Mpc}^{-1}$ for the present-day Hubble constant, $n_s = 0.96$ for the primordial spectral index and $\sigma_8 = 0.8$ for the normalization of the power spectrum. Resolution is increased within the selected regions by enlarging the number of particles and correspondingly adding higher-frequency modes from the power spectrum of the same cosmological model, by using the Zoomed Initial Condition technique (Tormen et al. 1997). The runs were carried out using the GADGET-3 code, a newer and more efficient version of the former GADGET-2 code (Springel 2005). In all simulations a Plummer-equivalent softening length for the computation of the gravitational force in the high-resolution region was fixed to $\epsilon = 5 h^{-1} \text{kpc}$ in physical units for the most recent redshifts ($z < 2$), while it was kept fixed in comoving units at earlier epochs. As for the computation of hydrodynamic forces, we assume the smoothed particle hydrodynamics smoothing length to reach a minimum allowed value of 0.5ϵ .

Besides a set of dDM-only simulations and a set of non-radiative (NR) hydrodynamical simulations, we also carried out two sets of radiative simulations (CSF and AGN). In these simulations radiative cooling rates are computed by following the procedure presented by Wiersma et al. (2009), including the effect of cosmic microwave background radiation and of UV/X-ray background radiation from quasars and galaxies (Haardt & Madau 2001). The contributions to cooling from 11 elements (H, He, C, N, O, Ne, Mg, Si, S, Ca, Fe) have been pre-computed using CLOUDY (Ferland et al. 1998) for an optically thin gas in (photo-)ionization equilibrium.

The CSF set of simulations includes star formation and the effect of feedback triggered by supernova (SN) explosions. As for the star formation model, gas particles above a given threshold density are treated as multiphase, so as to provide a sub-resolution description of the interstellar medium, according to the model originally described by Springel & Hernquist (2003). SNe II, SNe Ia, and low- and intermediate-mass stars contribute to the production of metals according to the model described by Tornatore et al. (2007): assuming a Chabrier initial mass function (Chabrier 2003) stars produce metals over the time scale determined by the mass-dependent life times of Padovani & Matteucci (1993). The effect of kinetic feedback triggered by SNe II is included according to the prescription by Springel & Hernquist (2003). In the CSF simulation set we assume $v_w = 500 \text{ km s}^{-1}$ for the velocity of the outflows, with a mass-upload rate that is two times the value of the local star formation rate.

The AGN set of simulations is carried out by including the same physical processes as in the CSF case, with a lower wind velocity of $v_w = 350 \text{ km s}^{-1}$, but also including the effect of AGN feedback. In this model, largely based on the original implementation of black-hole (BH) feedback by Springel et al. (2005), energy results from gas accretion onto supermassive BHs. BHs are included as sink particles, which grow in mass by gas accretion and merging with other BHs. Gas accretion

proceeds at a Bondi rate, and is limited by the Eddington rate. Once the accretion rate is computed for each BH particle, a stochastic criterion is used to select the surrounding gas particles to be accreted. Unlike in Springel et al. (2005), in which a selected gas particle contributes to accretion with all its mass, we included the possibility for a gas particle to accrete only with a slice of its mass, which corresponds to 1/4 of its original mass, thus providing a more continuous description of the accretion process (see also Fabjan et al. 2010). BH particles are initially seeded with a mass of $5 \times 10^8 h^{-1} M_\odot$. Seeding of BH particles takes place at the minimum of the potential of halos when they first reach a minimum friend-of-friend mass of $2.5 \times 10^{13} h^{-1} M_\odot$ (using a linking length of 0.16 in units of the mean inter-particle separation), with the further condition that such halos should contain a minimum mass fraction in stars of 0.02. This condition guarantees that substantial star formation took place in such halos and that seeding does not take place in structures linked together by the friend-of-friend algorithm, not corresponding to a real halo. A radiation efficiency parameter of $\epsilon_r = 0.1$ determines the amount of radiated energy extracted from gas accretion, in units of the rest-mass energy of the accreted gas, with the BH mass being correspondingly decreased by this amount. A fraction ϵ_f of this radiated energy is thermally coupled to the surrounding gas. We use $\epsilon_f = 0.1$ for this feedback efficiency, which increases to $\epsilon_f = 0.4$ when accretion enters in the quiescent “radio” mode and takes place at a rate smaller than 1/100 of the Eddington limit (e.g., Sijacki et al. 2007; Fabjan et al. 2010).

2.2. Simulated Catalog for the Intrinsic Analysis

The intrinsic analysis described in Section 3 is based on a set of 52 objects. Only the 24 largest clusters constitute a complete sample being the most massive halos identified within the parent cosmological box of $1 h^{-1} \text{Gpc}$. These were specifically selected for the purpose of comparing simulations of galaxy clusters with X-ray observations that are available for a fairly large number of massive, X-ray luminous objects. In order to extend the mass range over which to measure the $c-M$ relation, we include in our analysis also lower-mass systems, identified within a variety of different environments. The final sample includes the central clusters of each of 29 Lagrangian regions (24 centered on as many of the most massive clusters, plus 5 regions centered on lower-mass isolated systems), three halos selected from rich environments surrounding the massive clusters (regions containing more than 20 halos with virial mass larger than $5 \times 10^{13} h^{-1} M_\odot$), six halos from a poor environment (Lagrangian regions containing less than eight halos per region with mass larger than the same limit), and 14 halos lying in a medium-populated environment. The sample-covered mass interval is similar to that usually considered in observational works, with M_{200} ranging from $7.5 \times 10^{13} h^{-1} M_\odot$ to $2.5 \times 10^{15} h^{-1} M_\odot$. All clusters have been analyzed at redshift 0 (for comparison with other works present in literature) and 0.25 (for comparison with the X-ray sample of R12). Throughout the paper, we will focus on the $z = 0$ objects reporting our $z = 0.25$ results in the Appendix.

2.3. Synthetic Catalog

The synthetic X-ray catalog (R12) employed in Section 4 contains 60 event files related to three orthogonal projections

² $h = 0.72$ throughout the paper.

of 20 massive objects as part of the CSF sample at $z = 0.25$.³ The catalog has been created using the *X-Ray Map Simulator* (X-MAS; Gardini et al. 2004; Rasia et al. 2008) after the removal of the over-cooled particles identified in the density ($\rho[\text{gr}/\text{cm}^3]$) – temperature ($T[\text{keV}]$) plane that satisfy the condition $T < 3 \times 10^6 \rho^{0.25}$. This cut reduces the presence of small peaked clumps in the X-ray images without affecting the overall distributions of density, temperature, and X-ray luminosity (see Appendix of R12). The redistribution matrix function and ancillary response function adopted are those of *Chandra* ACIS-S3. The field of view is 16 arcmin, equivalent to $\sim 2.5 h^{-1}$ Mpc for our cosmology and redshift, and the exposure time is 100 ks. The metallicity is kept constant to 0.3 solar with respect to the tables of Anders & Grevesse (1989) with a small correction on the helium abundances to be consistent with the simulated hydrogen mass fraction. The galactic absorption, described by a *WABS* model, is fixed to $N_{\text{H}} = 5 \times 10^{-20} \text{ cm}^{-2}$. Along the line of sight, we consider the information of all the particles located up to $5 h^{-1}$ Mpc (in both directions) from the center of the object. The final event files avoid the inclusion of the background since this component does not influence the mass profile derivation (Rasia et al. 2006).

3. THE INTRINSIC c - M RELATION

3.1. Density Profiles and Fitting Procedure

To perform the tri-dimensional analysis of our simulated sample, we proceed by extracting the spherical mass profiles in 50 bins logarithmically spaced from $10 h^{-1}$ kpc to $5 h^{-1}$ Mpc and centered on the minimum of the potential well. For each cluster, all the bins external to $\approx 2\%$ of R_{200} have more than 1000 particles. This number represents the threshold for numerical convergence of the inner slope (Power et al. 2003). Following an observational approach, we fit our simulated profile with the NFW mass expression (Equation (2)) assuming a 10% error on the mass, a value consistent with the typical errors in observations (B07; E10) and previous analyses of synthetic X-ray catalogs (Meneghetti et al. 2010, R12). Using the values of ρ_s and r_s obtained from the fit of the density profiles, we compute the NFW masses at critical overdensity 200. We then compute the concentration using Equation (3). The 1σ static errors on the NFW mass and concentration are derived through the propagation of the errors on ρ_s and r_s applied to Equations (2) and (3), respectively. The c – M relation is, then, calculated using the LINMIX_ERR routine (Kelly 2007) in IDL to linearly fit the following expression:

$$\log_{10} c = \log_{10} c_0 + \alpha \times \log_{10} \frac{M_{\text{NFW}}}{5 \times 10^{14} h^{-1} M_{\odot}} + \epsilon_{\log} \quad (4)$$

The routine includes measurement-error information in both variables, utilizes a Bayesian approach, and returns a posteriori distributions of normalization ($\log_{10} c_0$), slope (α), and the variance of the intrinsic scatter (ϵ_{\log}) assumed to be log-normal (Dolag et al. 2004; De Boni et al. 2013) with mean equal to zero. For the reduced size of our sample we used the flag enabling the Metropolis–Hasting algorithm. From the distributions, the median values and their error, σ defined as the half-distance from the two values containing 68.27% of the distribution,⁴ are extracted. Subsequently, the normalization and its

statistical error are converted from logarithm to linear scale: $c_0 = 10^{\log_{10} c_0}$ and $\sigma_{c_0} = \ln(10) \times c_0 \times \sigma_{\log_{10} c_0}$. Finally, the statistical scatter is computed as

$$\sigma_{\text{stat}} = \sqrt{\frac{\sum_i [\sigma_{\log_{10}(c_i)}]^2}{N}} = \sqrt{\frac{\sum_i [\sigma_{(c_i)}/c_i/\ln(10)]^2}{N}}, \quad (5)$$

where c_i is the concentration of the i cluster, $\sigma_{(c_i)}$ its statistical error, and N the number of clusters considered.

The process is performed multiple times on the same object changing in each circumstance the radial range assumed (Section 3.3). For the hydrodynamical simulations (NR, CSF, and AGN), we analyze both the total mass profile and the DM-only profile.

3.2. Redefinition of the Sample

When studying the influence of the radial range (Section 3.3) and the baryonic physics (Section 3.4), we consider *only* the profiles that show a good consistency with the NFW description. In this way we exclude both objects that present one or more large substructures that produce a secondary peak in the density profile and halos that do not have a coherent concentration parameter associated. This a priori selection is not usually embraced in theoretical works, however, it is often implicitly adopted in observational samples, especially if they are focused on regular systems. The careful choice of the simulated clusters that need to be discarded is done on the basis of the NFW residuals:

$$\sigma_{\text{res}} = \sqrt{\frac{\sum_i^{N_{\text{bin}}} [\log_{10}(M_i) - \log_{10}(M_{\text{NFW},i})]^2}{N_{\text{bin}}}}. \quad (6)$$

For all situations considered (varying ICM physics or radial

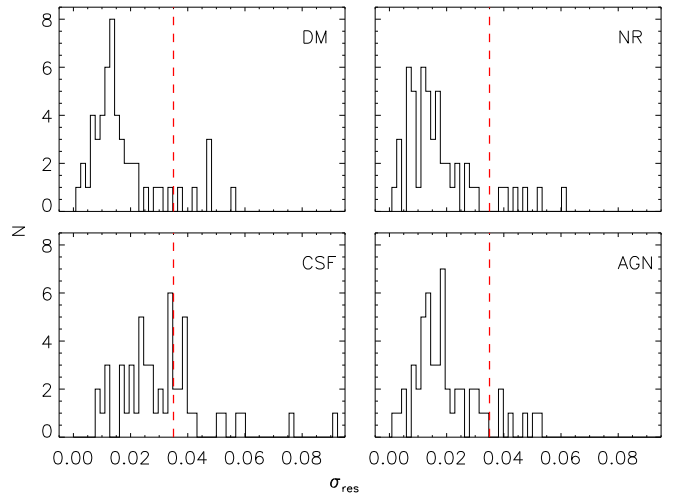


FIG. 1.— Distribution of residuals, σ_{res} , as defined in Eq.6 of the four physics and at redshift zero. The concentration is derived assuming the SIM radial range, $[0.06 - 1.27] \times R_{200}$, as defined in Section 3.3.1. Acceptable clusters have $\sigma_{\text{res}} < 0.035$ (values shown by a red dashed vertical line).

ranges) and for both redshifts, we study the distributions of the residuals and notice that the majority of the objects have residuals below 0.035 at $z = 0$ (see Figure 1) and 0.05 at $z = 0.25$. The residuals are significantly larger at $z = 0.25$ especially for the NR physics. Furthermore, at fixed redshift, the outliers are often the same objects despite the change of the simulated set or the fitting radial range. Per each redshift, we identify

³ Notice that X-ray synthetic catalog has a more restricted mass range with respect to the sample of the intrinsic analysis.

⁴ For a symmetric distribution this would be equivalent to the standard deviation.

these systems: nine clusters at $z = 0$ and at $z = 0.25$. The NR physics presents larger deviations because accreted substructures requires more time to virialize and thermalize under the NR physical condition (Dolag et al. 2009).

In the following, we decide to always exclude these identified systems and any other existing outliers (defined as having $\sigma_{\text{res}} > 0.035$ at $z = 0$ and $\sigma_{\text{res}} > 0.05$ at $z = 0.25$). The number of the remaining clusters is denoted by N and is listed in Tables 1–3. For each situation investigated, before deriving the $c-M$ relation, we check whether the excluded halos are spread across the mass range. When this does not happen (for example, if all objects below a certain mass disappear) we do not compute the $c-M$ relation because of the significant reduction in the sample mass range.

3.3. The Effect of the Radial-range Choice

3.3.1. Typical Theoretical and Observational Radial Range

Previous works demonstrated that the fitting radial range has some level of impact on the derived NFW concentration. For example, Rasia et al. (2006) showed that the concentration of a single cluster varies from ~ 5.3 to 7 (23% variation) when the outer radius moves from the virial radius to 20–30% of that radius. Using their X-ray observations on A2717, Gastaldello et al. (2007) warned of deriving the concentration parameter if the data do not extend beyond the measured scale radius. Fedeli (2012) stressed more the consequences of the choice of the inner radius: fitting from 1% of R_{200} induces a higher concentration, especially in small systems, than starting from 5% of R_{200} .

To evaluate the influence of the radial range assumed to fit the mass profile with the NFW formula, we begin by studying the DM sample. We first consider radial ranges that are ‘typically’ used in theory and X-ray studies, and then we move to a more general discussion.

Our references for theoretical works are Neto et al. (2007), Duffy et al. (2008, 2010) and Meneghetti & Rasia (2013). Their radial range used to fit the NFW formula is between 5 % and 100% of the virial radius, where the innermost limit was set to satisfy the requirement on the numerical convergence (Section 3.1 and Power et al. 2003). This interval is equal to $[0.06, 1.27] \times R_{200}$. We label this typical simulation radial range as SIM.

The X-ray radial range is, instead, linked to the one used in Ettori et al. (2010). The authors provided the radial boundaries used to compute the NFW best fit. The inner radius was constantly fixed to 50 kpc to exclude the impact of the central galaxy on the density profile, thus avoiding the stellar component influence. In our whole sample, this value is larger than $0.03 \times R_{200}$ fulfilling the numerical convergency requirement. E10 also furnished two outer radii, one associated with the surface brightness profile and the other with the spectroscopic temperature profile. Per each cluster, we select the minimum of the two and compare its values to the derived R_{500} . The resulting mean ratio was equal to 0.6.⁵ Concluding, we label the radial range from 50 kpc to $0.6 \times R_{500}$ ⁶ as X-ray. Furthermore, to account for recent X-ray observations reaching more external regions (e.g. Humphrey et al. 2012; Walker et al. 2013), we enlarge the outer boundary of the range where the analysis is carried out to 0.8 and $1 \times R_{500}$. In all the cases analyzed in Sec-

tion 3, the results, however, vary by only a few per-cent with respect to the results from the original X-ray radial range.

Considering both the SIM, and the X-ray, radial ranges, we fit the same DM cluster mass profiles, derive values of both NFW concentration and mass, and fit the $c-M$ relation (Equation (4)). For the $z = 0$ sample we provide in the first two rows of Table 1 the median values of the *posterior* distributions of the normalization, c_0 , and slope, α , as long as the rms values of the intrinsic-scatter, σ_{ellog} , and of the statistical scatter, σ_{stat} . The two slopes are consistent while the normalizations differ by more than 1σ : when a typical X-ray, radial range is used, the normalization increases by 10% with respect to the value of the theoretical radial range. Limiting the fit to inner parts of the mass profile produces an increase of the halo concentration at all mass scales. This is due to the combined effect of lowering both the internal and external boundaries. In this case, the innermost part of the profile weights very strongly. Indeed, within $100 h^{-1}$ kpc almost all the NFW X-ray best fitting parameters are larger than those obtained for the SIM, case. Comparing the concentrations, the scale radii, and the two R_{200} derived, we found that with respect to the SIM, radial range: (1) the X-ray, $R_{200}(= r_s \times c)$ is only 4% lower; (2) the X-ray, scale radii are significantly lower ($\sim 13\%$) and, consequently, (3) the X-ray, concentrations are higher ($\sim 16\%$). In both cases, the intrinsic scatter is around 10% with only a 3% statistical scatter. The intrinsic scatter is comparable to the values derived from observational data (B07, E10). The statistical scatter is instead slightly smaller than that reported by B07 (~ 0.06) and significantly smaller than that found by E10 in the analysis of their entire cluster sample. This disagreement is mostly due to the different methods used to derive the concentrations. In fact, the concentrations in E10 are obtained as best-fitting parameters that minimize the difference between the reconstructed temperature profile and the profile obtained from the spatially resolved X-ray spectroscopy. Meneghetti et al. (2010) showed that the concentration errors associated with this procedure are on average three times larger than those obtained via the direct NFW fit of the mass profile obtained by the forward method, i.e., by applying the equation of hydrostatic equilibrium on the fitted emission measure and temperature profiles. However, we note that the statistical and intrinsic scatters of the best-determined relaxed systems analyzed by E10 are 3% and 7%, thus in agreement with our results.

TABLE 1

CONCENTRATION-MASS BEST-FIT PARAMETERS WITH 1σ ERROR OF THE DM SAMPLE AT REDSHIFT $z = 0$. APART THE X-RAY RADIAL RANGE FIXED BETWEEN 50 KPC AND $0.6 \times R_{500}$, ALL REMAINING RADIAL RANGES ARE DEFINED IN UNITS OF R_{200} , WITH SIM= $[0.06 - 1.27] \times R_{200}$. N IS THE NUMBER OF OBJECTS SATISFYING THE CONDITION ON THE NFW RESIDUALS ($\sigma_{\text{res}} < 0.035$).

	N	α	c_0	$\sigma_{\text{ellog}}, \sigma_{\text{stat}}$
SIM	43	-0.17 ± 0.04	3.70 ± 0.14	0.10, 0.03
X-ray	42	-0.15 ± 0.05	4.06 ± 0.14	0.09, 0.03
0.06–0.4	43	-0.25 ± 0.07	3.85 ± 0.16	0.07, 0.05
0.06–2.0	43	-0.15 ± 0.04	3.73 ± 0.13	0.10, 0.02
0.03–1.27	42	-0.13 ± 0.04	3.82 ± 0.14	0.10, 0.02
0.2–1.27	43	-0.31 ± 0.10	3.57 ± 0.19	0.07, 0.06

⁵ In Ettori et al. (2010) two different R_{500} radii were reported according to two different derivations of the mass profiles. For our purpose, the variation between these is minimal, as we tested.

⁶ This value corresponds roughly to $0.4 \times R_{200}$ for our objects.

3.3.2. Generalization of the adopted radial range

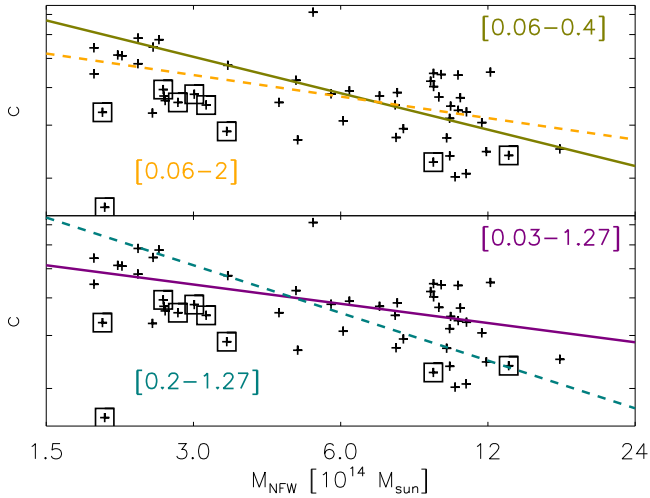


FIG. 2.— Relation between NFW concentrations and masses computed for the DM halos assuming the SIM radial range. Black squares indicate the 9 clusters excluded for their large residuals ($\sigma_{\text{res}} > 0.035$). The lines represent the fits to four different sets of concentration and mass values extracted by adopting four separate radial ranges (the 4 sets of points are omitted for clarity). With respect to the SIM radial range, we vary the external radius from $0.4 \times R_{200}$ (solid green line) to $2 \times R_{200}$ (dashed orange line) in the top panel, and the internal radius from 0.03 (solid purple line) to $0.2 \times R_{200}$ (dashed light blue line) in the bottom panel.

To broaden the discussion about the radial ranges, we explore some variation on the external and the internal radii with respect to the SIM, radial range. The results are shown in Figure 2 and listed in the lower part of Table 1. For clarity, we show the cluster points only for the SIM, radial range. In the top panel, the inner radius is constantly equal to $0.06 \times R_{200}$, while the external one varies from $0.4 \times R_{200}$ (solid green line) to $2 \times R_{200}$ (dashed orange line). The first number is close to the X-ray external radius ($0.6 \times R_{500} \sim 0.4 \times R_{200}$), while the second extends beyond the virial region. Carrying the analysis out to such larger radii (not reachable by optical and X-ray observations) aimed at testing the influence of the possible presence of filaments and accreting structures in the outskirts of clusters. From this plot, it appears that both slopes and normalization slightly increase when the external radius becomes smaller and closer to the X-ray, limit.

Even if the changes are very small, we tested the origin of this trend. We found that halos with different masses react differently to changes of the radial fitting: smaller halos play the major role. For example, the parameters ρ_s and r_s , of our most massive clusters ($M_{\text{true}} > 10^{15} h^{-1} M_{\odot}$)⁷ do not depend on the radial range chosen implying an averaged small variation on the NFW masses (5%) and concentrations (2%). Our smallest clusters ($M_{\text{true}} < 1.5 \times 10^{14} h^{-1} M_{\odot}$), instead, show a change in the scaling radius and in the normalization of $\sim 10\%$ each. The consequence of using the narrowest radial range is to produce a 5.5% larger concentration and 7.5% smaller NFW mass with a shift not parallel to the SIM, c_M relation but almost orthogonal to it, thereby causing the overall change of the slope. We infer that the radial range might play a more relevant role whenever the sample extends to small halos.

⁷ We indicate with M_{true} the true mass of the simulated objects within R_{200} . Notice that it might differ from the NFW masses reported in the various figures.

The other scenario presented in the lower panel of the same Figure 2 regards the change on the inner radius from $0.03 \times R_{200}$ (dashed blue line) to $0.2 \times R_{200}$ (solid purple line), while the external radius is kept fixed at $1.27 \times R_{200}$. With respect to the SIM radial range, excluding a significant portion of the inner profile (with a cut similar to that applied in weak-lensing studies) causes an increase of the slope by almost a factor of 2. Extending the fit to inner regions (i.e., to values comparable to the X-ray, inner radius), instead, slightly increases the normalizations as previously noticed comparing the X-ray, and SIM radial ranges. The objects responsible for the difference between the two relations are the most massive clusters, thus at variance with the above considered case. Moving from the typical X-ray inner radius to the typical weak-lensing inner radius, concentrations and masses change by 8% and 5%, respectively, for the largest clusters, and only by 3% and 1% for the smallest ones.

In all the situations examined, however, the variation of the $c-M$ relation is not enough to explain the differences between the slopes of the simulated and observed relations of SA07 and E10.

3.4. The Effect of Baryons

To evaluate the influence of baryons and of the baryonic physics on the $c-M$ relation, we fit the NFW formula (Equation (2)) to the mass profiles of the hydro simulations using all the radial ranges discussed above (SIM, X-ray, and the four cases of Figure 2 and Table 1). Besides the total mass profile, we consider in this section also the DM-only mass profile, that is, the mass profiles associated only with the dark-matter component within the hydrodynamical simulations. Our results are summarized in Table 2 and described in the following.

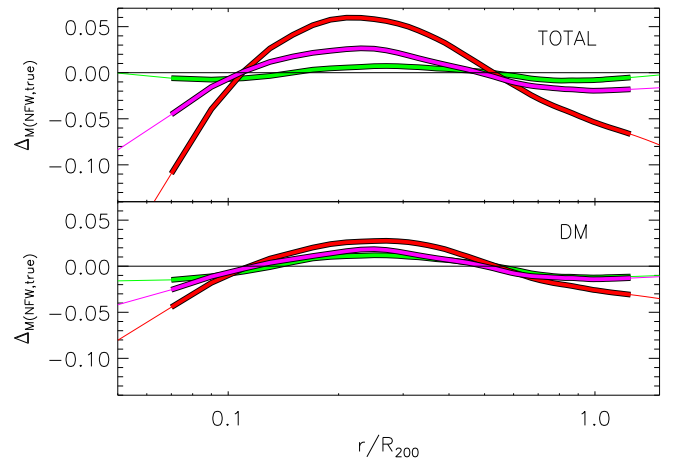


FIG. 3.— Profiles of the residuals $\Delta_{M(\text{NFW},\text{true})} = (M_{\text{NFW}} - M_{\text{true}}) / M_{\text{true}}$ computed for the hydro simulations (NR in green, CSF in red, and AGN in magenta), assuming the SIM radial range, at redshift zero. In the top panel, the NFW fit is applied to the total mass profile, while in the bottom panel the mass profiles of the only dark-matter particles are considered.

3.4.1. Deviation from the NFW formula

From Table 2, we note that the number of clusters, N , whose mass profiles are well fitted by the NFW expression (see Section 3.1) is heavily reduced for the CSF sample. This is caused by the large deviation from the NFW profile especially in the innermost regions. This can be seen from Figure 3, where we plot

TABLE 2

CONCENTRATION–MASS BEST-FIT PARAMETERS WITH 1σ ERROR OF THE HYDRODYNAMICAL SAMPLES AT REDSHIFT $z=0$. FITTING RADIAL RANGES AND SYMBOLS ARE AS IN TABLE 1. LEFT: RESULTS OBTAINED FROM THE TOTAL DENSITY PROFILE; RIGHT: RESULTS RELATED TO THE DM–ONLY DENSITY PROFILE.

	NR				DM in NR			
	N	α	c_0	$\sigma_{\epsilon_{\log}}, \sigma_{\text{stat}}$	N	α	c_0	$\sigma_{\epsilon_{\log}}, \sigma_{\text{stat}}$
SIM	43	-0.17 ± 0.05	3.98 ± 0.17	$0.12, 0.03$	43	-0.18 ± 0.05	3.66 ± 0.16	$0.11, 0.03$
X-ray	42	-0.19 ± 0.05	4.06 ± 0.19	$0.12, 0.03$	42	-0.19 ± 0.06	3.86 ± 0.17	$0.11, 0.03$
[0.06–0.4]	43	-0.27 ± 0.09	4.05 ± 0.21	$0.10, 0.05$	41	-0.28 ± 0.09	3.69 ± 0.20	$0.09, 0.05$
[0.06–2.0]	41	-0.14 ± 0.04	4.10 ± 0.16	$0.10, 0.02$	42	-0.15 ± 0.04	3.70 ± 0.14	$0.10, 0.02$
[0.03–1.27]	41	-0.14 ± 0.04	4.02 ± 0.17	$0.12, 0.02$	41	-0.15 ± 0.04	3.75 ± 0.15	$0.11, 0.02$
[0.21–1.27]	43	-0.32 ± 0.12	3.92 ± 0.22	$0.08, 0.06$	43	-0.34 ± 0.11	3.45 ± 0.20	$0.07, 0.06$
	CSF				DM in CSF			
	N	α	c_0	$\sigma_{\epsilon_{\log}}, \sigma_{\text{stat}}$	N	α	c_0	$\sigma_{\epsilon_{\log}}, \sigma_{\text{stat}}$
SIM	40	-0.21 ± 0.05	4.76 ± 0.21	$0.11, 0.03$	43	-0.17 ± 0.04	3.86 ± 0.16	$0.11, 0.03$
X-ray	–	–	–	–	42	-0.21 ± 0.05	4.57 ± 0.16	$0.07, 0.03$
[0.06–0.4]	43	-0.30 ± 0.05	5.53 ± 0.26	$0.06, 0.03$	43	-0.30 ± 0.08	4.04 ± 0.21	$0.07, 0.04$
[0.06–2.0]	36	-0.20 ± 0.04	4.86 ± 0.18	$0.10, 0.04$	43	-0.16 ± 0.04	3.91 ± 0.15	$0.10, 0.02$
[0.03–1.27]	–	–	–	–	39	-0.18 ± 0.04	4.18 ± 0.16	$0.09, 0.02$
[0.21–1.27]	43	-0.33 ± 0.10	4.08 ± 0.22	$0.07, 0.06$	43	-0.33 ± 0.11	3.46 ± 0.20	$0.07, 0.06$
	AGN				DM in AGN			
	N	α	c_0	$\sigma_{\epsilon_{\log}}, \sigma_{\text{stat}}$	N	α	c_0	$\sigma_{\epsilon_{\log}}, \sigma_{\text{stat}}$
SIM	43	-0.13 ± 0.04	3.86 ± 0.16	$0.11, 0.03$	42	-0.14 ± 0.04	3.57 ± 0.15	$0.11, 0.03$
X-ray	37	-0.14 ± 0.05	4.85 ± 0.21	$0.10, 0.03$	43	-0.16 ± 0.05	3.45 ± 0.15	$0.11, 0.04$
[0.06–0.4]	43	-0.26 ± 0.08	4.13 ± 0.21	$0.10, 0.05$	43	-0.25 ± 0.09	3.66 ± 0.20	$0.09, 0.05$
[0.06–2.0]	41	-0.11 ± 0.04	3.91 ± 0.15	$0.10, 0.02$	41	-0.12 ± 0.04	3.62 ± 0.14	$0.10, 0.02$
[0.03–1.27]	24	-0.14 ± 0.04	4.21 ± 0.18	$0.11, 0.02$	40	-0.13 ± 0.04	3.71 ± 0.15	$0.11, 0.02$
[0.21–1.27]	43	-0.27 ± 0.13	3.65 ± 0.19	$0.09, 0.06$	43	-0.32 ± 0.12	3.31 ± 0.20	$0.08, 0.06$

the average profiles of the NFW-mass deviations from the true mass profile: $\Delta_{M(\text{NFW}, \text{true})} = (M_{\text{NFW}} - M_{\text{true}})/M_{\text{true}}$. The figure is built excluding the nine systems with large residuals. Even so, the CSF clusters (in red) largely depart from a pure NFW at the center. The NR clusters (in green) are very well represented by the NFW formula showing almost zero deviations at all radii. The AGN runs are halfway: including radiative cooling, as the CSF runs, they also have central profiles steeper than an NFW profile and than the NR clusters. However, the presence of AGNs, which push a considerable amount of gas toward more external radii, reduces this effect with respect to the CSF simulations (Fabjan et al. 2010).

The condensation of baryons in the center is very efficient in less massive objects. Indeed, almost all our CSF groups with $M_{\text{true}} < 2 \times 10^{14} h^{-1} M_{\odot}$ have residuals $\sigma > 0.035$ when the fit is extended to small innermost limits such as $0.03 \times R_{200}$ and 50 kpc. The exclusion of all these systems implies a drastic reduction of the mass range impeding to robustly derive the $c-M$ relation. The statistics for these two cases being quite different, we do not report the corresponding values of the fitting parameters in Table 2.

From the bottom panel of Figure 3, we confirm that the NFW is an excellent description of the mass profile of the DM component within hydrodynamical simulations. Similar results for lower mass systems were obtained by Duffy et al. (2010). This feature persists in all studies obtained by varying the radial range and the physics adopted, as witnessed by the value of N in the right part of Table 2.

3.4.2. Comparison with the DM Analysis: Slope

The results of the hydrodynamical simulations (Table 2) indicate that the slopes of the $c-M$ relations are always consistent within 1σ error with the DM slopes (Table 1). The only major change lies in a more pronounced increase of the slope when either the internal or the external limit of the radial range is modified. For instance, the difference in the AGN case is twice as much as the variation in the DM case when the external limit changes from the limit assumed in the SIM case to $0.4 \times R_{200}$. The reason for this behavior can be understood from Figure 4, where we plot the averaged density profiles of the least massive (black line) and most massive (red line) clusters renormalized to coincide at $0.5 \times R_{200}$. The profiles are not exactly self-similar: least massive groups are on average more concentrated than largest clusters. In the bottom panel, we show how much concentrations and NFW masses vary in relation to the external radius. Most points are lying in a precise location because the concentrations and masses of the two cases refer to the same potential well as we are modifying only the fitting radial range. A certain degeneracy between the parameters is, therefore, expected. We find that our most massive systems ($M_{\text{true}} > 10^{15} h^{-1} M_{\odot}$), on average, maintain the same concentration and mass despite the change of the radial range. On the other hand, the smallest clusters ($M_{\text{true}} < 1.5 \times 10^{14} h^{-1} M_{\odot}$) show a drop in concentration and an increase in mass when extending the fit beyond the virial radius.

3.4.3. Comparison with the DM Analysis: Normalization

The largest difference between the $c-M$ relations predicted by hydrodynamical and by DM simulations lies in the normalization that shows a systematic increase (Table 2) of 5% – 10%

for the NR runs, 15% – 50% for the CSF runs, and of 25% – 40% for the AGN runs. The radiative runs are those showing the largest deviations with respect to the DM case, especially when we reduce the outer limit of the radial range to $0.4 \times R_{200}$. This result is shown in the top panel of Figure 5, where, similarly to what is shown in the lower box of Figure 4, we are reporting the variation in NFW concentrations and masses moving from the DM runs to the hydrodynamical simulations using the SIM radial range for $z = 0$ systems. The CSF simulations produced a steeper relation and a higher normalization: the inclusion of baryons without a strong feedback induces an increase of the concentration at all mass scales (see lower panel in the figure). The effect is mitigated, if not completely canceled, when we include the strong feedback produced by the AGNs. From the bottom panel, we can evince that the slope of AGN and NR is very similar to the DM one (both sets of green and magenta points are parallel to the DM black horizontal line). Finally, we observe that the deviations in both concentration and mass are correlated (top panel), implying that even if the simulated underlying physics is changed, the cluster mass profiles are not amply modified.

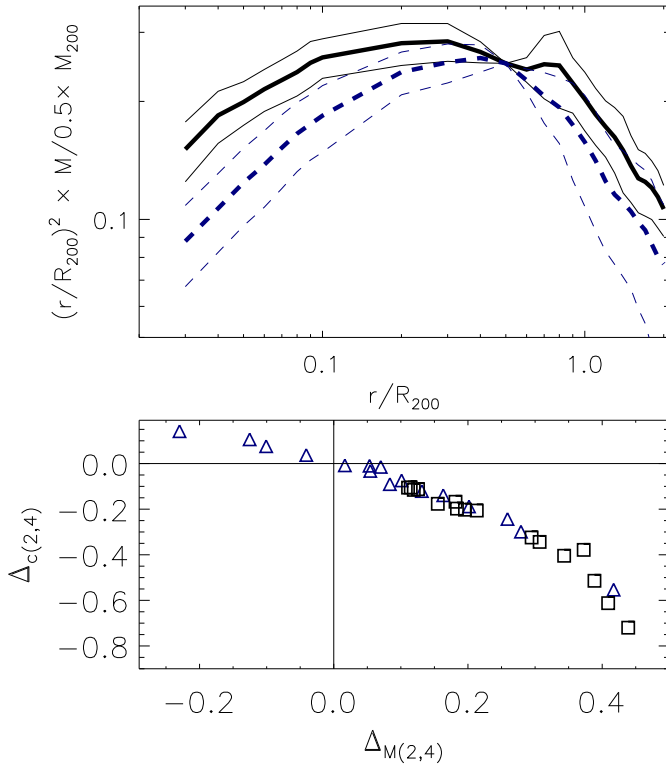


FIG. 4.— Top panel: averaged mass profiles of the 17 least (black solid line) and the 17 most (light blue dashed line) massive clusters of the AGN sample, multiplied by the radius squared and normalized at $0.5 \times R_{200}$. The thin lines represent the 1σ range with respect to the mean value. *Quite clearly, the two profiles are not self-similar.* Bottom panel: difference between the NFW concentrations and masses: computed assuming two different radial ranges: $[0.06-2] \times R_{200}$ and $[0.06-0.4] \times R_{200}$. Naming the concentrations and masses as c_2 and M_2 in the first case and c_4 and M_4 in the second case, we plot the quantities $\Delta_{c_{2,4}} = (c_2 - c_4)/c_2$ and $\Delta_{M_{2,4}} = (M_2 - M_4)/M_2$. Black squares refer to the 17 least massive objects while light blue triangles refer to the 17 most massive clusters. *The radial range chosen has a larger impact on the smallest clusters.*

3.4.4. Comparison with Previous Theoretical Works

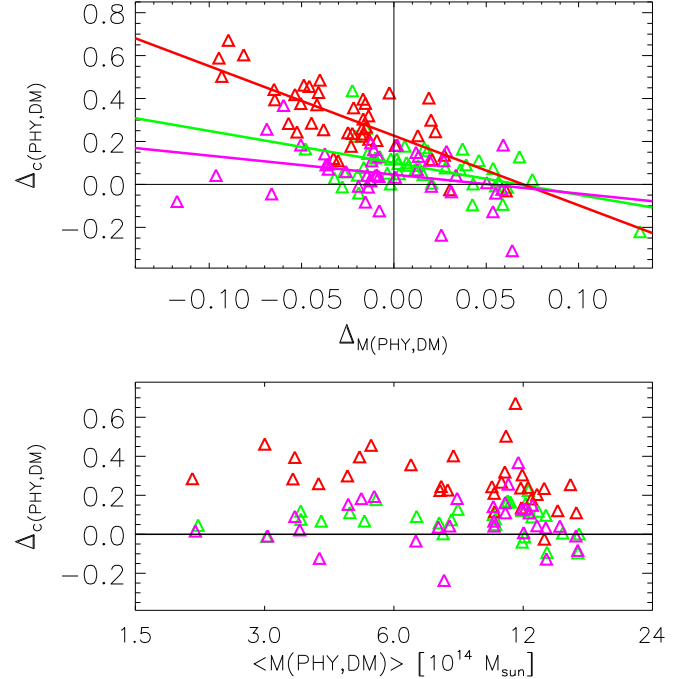


FIG. 5.— Top panel: variation in the NFW concentrations and masses when the quantities are computed in the hydrodynamical simulations with respect to the DM runs. Red, green, and magenta triangles represent CSF, NR, and AGN results, respectively, assuming the SIM radial range. Bottom panel: the concentration shift is shown in function of the average NFW mass, calculated as the mean of the DM and PHY masses.

Rudd et al. (2008), studying the influence of baryons on the matter power spectrum, analyzed how baryons affect density profiles and concentrations. Their results are very similar to ours: NR simulations have a concentration boosted by 5%-10% while simulations with gas cooling, star formation, and SN feedback present a larger difference (between 20% and 50%). Comparable values have been found by De Boni et al. (2013), who also measured small variations associated with the specific dark energy model considered.

Our results on the similarity between the concentration–mass relations for AGN and DM simulations confirm the results found by Duffy et al. (2010) for the largest halos in their simulations ($M \sim 10^{14} h^{-1} M_{\odot}$) and extend to more massive clusters.

3.4.5. Comparison with Previous Observational Works

The comparison with the three reference X-ray analyses by B07, SA07, and E10, is carried out using the three scaling relations re-derived by Fedeli (2012). The original papers adopted a Λ CDM cosmology with $h = 0.7$ and $\Omega_M = 0.3$. The first two works reported their measurements to the virial radius, the latter to R_{200} , and all assumed various modeling for the redshift evolution. In order to homogenize the results presented in the above observational analyses, Fedeli (2012) adopted the following approach: (1) extrapolated all the results to the overdensity $\Delta_c = 200$ (from Hu & Kravtsov 2003); (2) assumed the best-fitting cosmological model from the WMAP-7 analysis (Komatsu et al. 2011), similar to that assumed by our simulations; (3) removed any redshift dependence of the relation, and (4) chose a fixed pivot point at $5 \times 10^{14} h^{-1} M_{\odot}$, as we do.

We refer to the X-ray papers for a complete description of the samples, here, we summarize the salient points: B07 studied 39 regular objects with masses from $6 \times 10^{12} M_{\odot}$

to $2 \times 10^{15} M_{\odot}$. The core of their sample resides in early-type galaxies and groups with 16 systems of their sample with masses below $10^{14} M_{\odot}$. To these they added the massive clusters from the sample of Pointecouteau et al. (2005) and Vikhlinin et al. (2006). Restricting their analysis to only clusters with mass above $10^{14} M_{\odot}$, B07 confirmed what was previously found by the latter works.

SA07 used 34 massive halos having mass-weighted temperatures within R_{2500} above 5 keV and showing regular X-ray isoflux contours and minimal isophote centroid variations. Most of the X-ray information is contained in R_{2500} ($\sim 0.3 \times R_{200}$). Finally, E10 considered 44 very luminous nearby clusters with a minimum mass of $10^{14} M_{\odot}$ and defined a subset of 11 low-entropy core systems as representative of regular objects.

S07 and E10 selected their clusters on the basis of the X-ray luminosity. The X-ray analysis differs among the three works as it does the fitting of the NFW functional form: B07 fitted the dark matter plus stellar mass profile, SA07 used the total mass profiles, while E10 considered only the DM profile (subtracting the gas and excluding the central regions where the stellar component dominates). These choices partially explain the differences among the observational results. Another important component is the sample selection. For example, selecting only low-entropy systems within their sample, E10 found a slope 60% lower than considering the full ensemble of clusters.

Figure 6 confirms that changing the gas physics does not lead to significant changes in the slope of the concentration–mass relation, using either the SIM or the X-ray radial range. The highest slope values, obtained for CSF clusters, are only 23% higher than the DM slope and are significantly ($> 1\sigma$) smaller than the value found by E10 and only marginally consistent with SA07. On the other hand the slope derived by B07 is comparable to the one from our runs. As a note of caution, however, we remind that more than half of the observational sample analyzed has mass below our lower limit.

The normalization is affected by a larger degree by the change of the baryonic physics, even if it never reaches the normalization of SA0, the only observational work based on fitting the NFW formula to the total mass profile. The normalizations of the DM run are consistent with the value derived by Ettori et al. (2010).

As a final remark, the intrinsic and the statistical scatters of the hydrodynamical simulations are almost identical to those of the DM runs (see also Section 3.3).

To conclude this section, we would like to point out that the $c-M$ relation derived from the mass profiles of the DM particles within the hydrodynamical simulations exhibits normalization and slope values very similar among them and extremely close to those obtained from the pure N -body simulations. This result, joined with the fact that the DM profiles are always well represented by an NFW (lower panel of Figure 3), signifies that the best strategy to use in observations would be to compute the NFW concentration from the DM profile obtained by subtracting both the gas and stellar component from the total mass profiles (Newman et al. 2013).

4. THE OBSERVED C-M RELATION

4.1. Synthetic X-Ray Analysis

In this section we derive the $c-M$ relation from the synthetic X-ray cluster catalogue presented in R12 and compare it with the respective intrinsic relation. To this purpose, we plot three sets

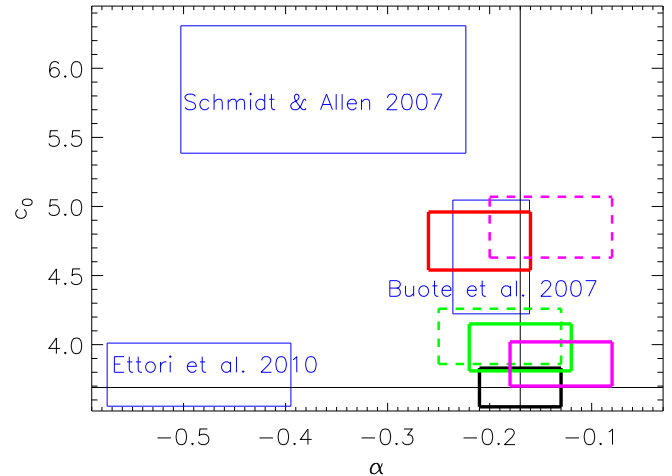


FIG. 6.— Normalization, c_0 , and slope, α , of the $c-M$ relations derived in the X-ray works present in literature (in blue) and in this paper (black, green, red, and magenta represent results derived from DM, NR, CSF, and AGN runs, respectively). Solid and dashed lines refer to results by fitting in the SIM and X-ray radial ranges, respectively. The size of the boxes represents the 1σ variation.

of points in Figure 7:

- c_i, M_i are the *intrinsic* parameters (black asterisks). The values are those of the 20 massive CSF clusters in common with the synthetic X-ray catalogue and analyzed using the SIM radial range at $z = 0.25$.
- c_{he}, M_{he} are derived from the 3D mass profiles obtained by including in the hydrostatic equilibrium equation the true 3D gas density profile and the true 3D mass-weighted temperature profile. These values are similarly obtained assuming the SIM, radial range (black crosses). The $c-M$ relation and its 1σ variation are shown by the black dashed line and cyan shaded region.
- c_X, M_X are the values derived from the X-ray analysis. In R12, the X-ray mass profiles have been derived following the *forward* method (Vikhlinin et al. 2006; Meneghetti et al. 2010): two fitting formulae have been adopted to fit the surface brightness and temperature profiles. The analytic best fits have been de-projected, and the mass calculated under the assumption of spherical symmetry and hydrostatic equilibrium. We adopted the mass profiles therein derived to fit the NFW formulae using Equation (2) and Equation (3) in the radial range probed by the X-ray analysis performed in R12. In this setting, the errors on the masses are taken directly from the X-ray analysis output. They typically span from 10%-12% in the most central bins to $\sim 5\%$ close to R_{500} , a value similar to those in the literature (Vikhlinin et al. 2009, E10). The NFW concentrations and masses of the fitting profiles that agree within 1σ with the X-ray hydrostatic mass profiles are shown in the figure with diamond symbols. The c_X-M_X relation and its 1σ scatter are shown with dark green and gray shaded regions, respectively. In green, we plot the results for our *disturbed* systems as defined in Rasia et al. (2013).⁸ Furthermore, we show in red results for the remaining systems, along

⁸ See figures in that paper's Appendix for the cluster images.

with the corresponding 1σ errors on concentration and NFW mass. The best fit to their c – M relations is plotted with the solid red line. The shaded yellow region represents the 1σ range of variation. As found by SA07, the NFW formula is generally a good description of our non-disturbed X-ray data: only one system presents a residual above 0.035.

The concentration–mass relations obtained by following different methods have *significantly* different slopes, ranging from $\alpha = 0.04 \pm 0.31$ in the case of $(c_{he} - M_{he})$ to -1.31 ± 0.57 in the case of the $(c_x - M_x)$ for regular-only systems. In this comparison, the intrinsic scatters ($\sim 15\%$), the statistical scatters ($\sim 2\%$), and the normalizations ($c_0 \sim 5$ – 5.5) are similar. Including the *disturbed* objects we still find a negative slope, $\alpha = -0.45 \pm 0.49$, with a decrease of the normalization, $c_0 = 3.91 \pm 0.39$, and a doubling of the intrinsic scatter, 25%, but no significant variation of the statistical scatter.

We proceed by analyzing separately two effects induced by (1) the assumption of the hydrostatic equilibrium and (2) the X-ray oriented approach and analysis.

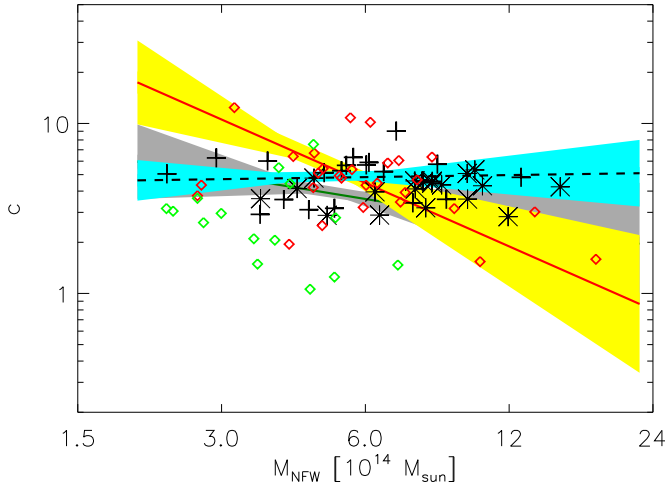


FIG. 7.— Values of concentration and mass from the 3D intrinsic mass profiles (c_i, M_i ; black asterisks), from the mass profiles derived by applying the hydrostatic equilibrium to the 3D gas density and 3D mass-weighted-temperature profile (c_{he}, M_{he} ; black crosses), and from the X-ray mass profile of R12 (c_x, M_x ; diamonds). In green we plot the values of *disturbed systems* as defined by Rasia et al. (2013) while the red colors refer to the remaining objects. The $c_{he} - M_{he}$, $c_x - M_x$, and non-disturbed-cluster $c_x - M_x$ relations are shown with dashed black, solid green, and solid red line, respectively. The corresponding 1σ ranges of variation are shown with the cyan, gray and yellow shaded regions.

4.2. Deviation Caused by the Hydrostatic Equilibrium Assumption

In the top panel of Figure 8 we show how much concentrations and masses vary when we introduce the hydrostatic equilibrium assumption in our *intrinsic* analysis. In this case we define $\Delta_{c(he,i)} = (c_{he} - c_i)/c_i$ and $\Delta_{M(he,i)} = (M_{he} - M_i)/M_i$, where i and he indicate values shown in Figure 7 by asterisks and crosses, respectively. In average, the two masses show a difference of 25%, with M_{he} lower than M_i . This value is in agreement with the results on the masses presented in R12 (red line in their Figure 6), confirming that the NFW fitting procedure is not introducing any extra bias. The concentrations show a discrepancy of 20% in the other direction without any specific

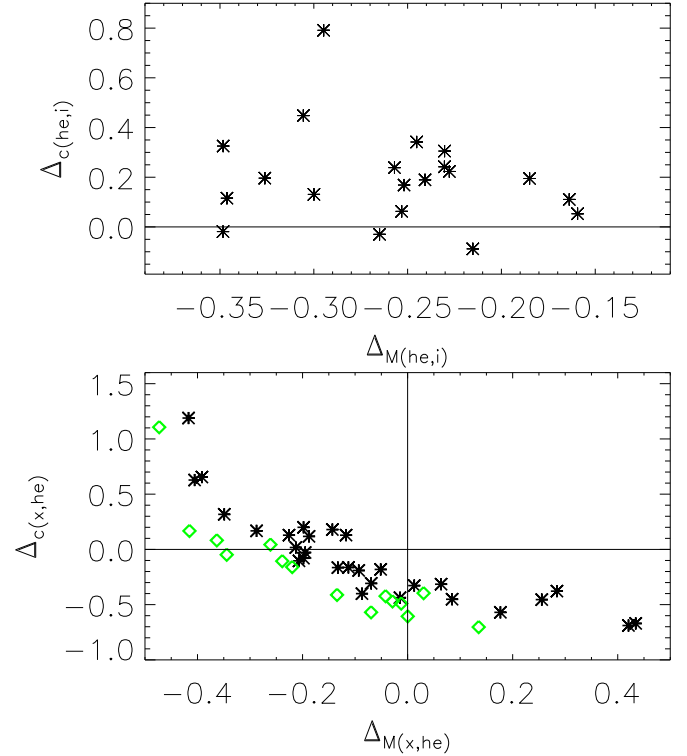


FIG. 8.— Deviations in concentrations and in masses. Top panel: differences in the concentrations obtained from the intrinsic and from the hydrostatic approaches are plotted against the corresponding differences in mass. Bottom panel: the same as in the top panel, but when comparing results from the hydrostatic analysis and from the X-ray approach. Disturbed systems are shown with green diamonds. Horizontal and vertical lines show the case of no-variation. *Irregular systems* show a larger shift in both concentration and mass.

correlation with either the mass of the systems, M_i , or the mass deviations, $\Delta_{M(he,i)}$. Consequentially, we measure 30%–40% larger normalization for the c – M relation $c_{he} - M_{he}$ when we assume the hydrostatic equilibrium, but we do not witness any change either in slope or in scatter (see also Lau et al. 2009).

The phenomenon emphasizes that the lack of hydrostatic equilibrium in each system increases with the radius (Rasia et al. 2004, 2006; Lau et al. 2009; Rasia et al. 2012; Khedekar et al. 2013; Battaglia et al. 2012). The profiles of M_{he} are closer to the true mass profile at the center and diverge more in the external region, automatically producing a more concentrated profile. The effect, however, is not sensible to the mass of the object, as we deduce from the fact that the slope of the c – M relation does not vary. This consideration confirms the results by Piffaretti & Valdarnini (2008), who, using a more numerous sample (above 100 objects) and a larger mass range, found a negligible dependence on the mass of the hydrostatic-mass bias.

4.3. Deviation Caused by the X-Ray Approach

The outcomes differ when we move to compare the intrinsic hydrostatic values (c_{he} and M_{he}) with the X-ray-derived one (c_x and M_x). A significant increase of dispersion on both concentrations and masses is present: most clusters at high (low) mass have a lower (higher) concentration producing a clear steepening of the relation. The deviations $\Delta_{c(x,he)} = (c_x - c_{he})/c_{he}$ and $\Delta_{M(x,he)} = (M_x - M_{he})/M_{he}$ are shown in the bottom panel of Figure 8.

The majority of the NFW masses from the X-ray data present

a further reduction, with a median value of -12% . The extra drop is caused by the temperature bias affecting this sample: the spectroscopic X-ray temperatures are lower than the mass-weighted ones because of dishomogeneity in the temperature distribution (R12).

The X-ray concentrations are significantly below the values derived from the 3D intrinsic profiles. The median deviation for the whole sample is -16% and shows dependence on the X-ray morphology. In Figure 8, we mark with green diamonds the systems belonging to the *disturbed* class. The average concentration deviation for the sub-sample of disturbed systems reaches -40% .

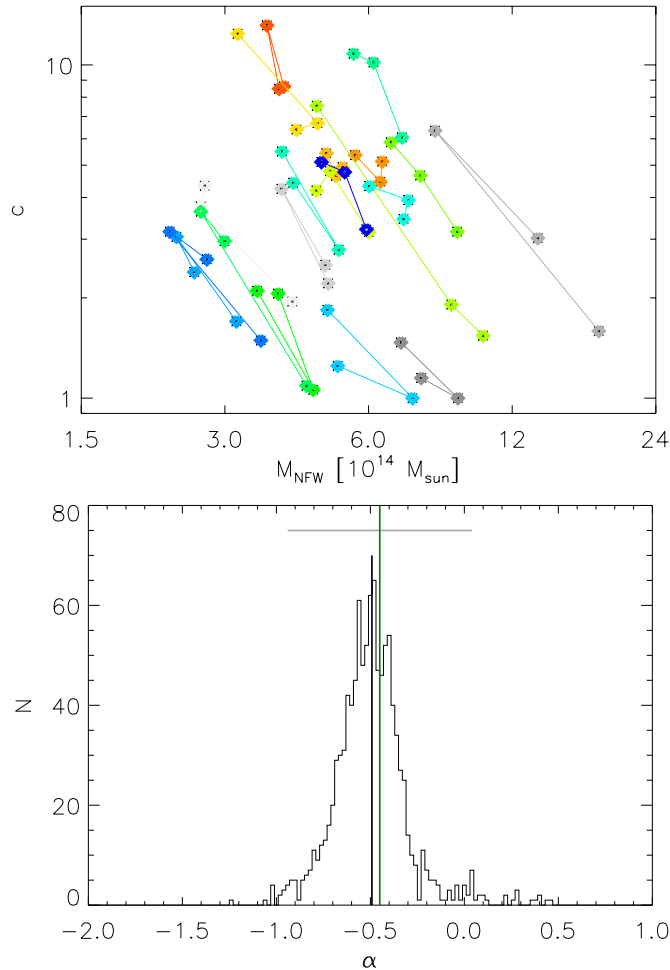


FIG. 9.— Top panel: the concentrations and the masses of the synthetic X-ray catalogue. Each color refers to an individual cluster whose 3 projections are connected by a line. Bottom panel: Distribution of the slope of the concentration-mass relation for 1,000 re-samplings of the 20 clusters produced by randomly selecting one of their line-of-sight projection. Black and green vertical lines correspond respectively to the median value of the distribution and the slope derived from the X-ray sample with 1σ error shown with the gray horizontal line. This plot demonstrates that there is less than 4% of probability of obtaining a slope equal to or smaller than the intrinsic value (equal to 0.04).

4.4. Testing Degeneracy between Parameters

The steepening of the relation might be a spurious effect originating from the fact that the 60 points are not completely independent; each single cluster is, instead, represented three times. Our concern is instigated by our previous results (Figures 4 and

5), suggesting degeneracy between NFW masses and concentrations once they are derived from the similar potential wells using slightly different procedural settings (either radial range or simulation set or, in this context, separate projections).

In the top panel of Figure 9, the set of points c_x, M_x are plotted with a choice of color that helps the identification of the three projections of the same object. Notice that almost always, with only two exceptions, clusters are classified as disturbed in all three projections. Clearly, this degeneracy is present. What needs to be tested is whether the direction of the degeneracy is parallel to the relation obtained by using only one projection or it is orthogonal and, thus, steepens the relation.

To test this, we generate 2,000 possible combinations of our 20 objects. Our resampling is built by randomly selecting only one of the three available line-of-sight projections per cluster. In this fashion, we are avoiding the degeneracy caused by having ‘same-potential’ systems in the sample. This approach is more indicated than some resampling methods such as *bootstrap* or *jackknife* since their main assumption – independency of the 60 measurements – is definitely not satisfied in our case. For each set, we derive the $c-M$ relation. The distribution of the ~ 1000 slopes with associated error less than 1 is shown in the bottom panel of Figure 9.

The X-ray slope of the c_x-M_x relation (green vertical line) is exactly in the middle of the distribution, meaning that the most probable slope obtained by the 20 objects is almost the same as that obtained from the enlarged sample of 60 images. From the histogram, we find that there is less than 4% probability to find a slope as large as that obtained from the analysis based on hydrostatic equilibrium as a random realization from the distribution obtained from the re-samplings of the 20 objects. This test, therefore, reassures that we are not introducing an extra bias from our sample.

4.5. Understanding the Observational-like $c-M$ Relation

Investigating, further, the reason for the steepening of the relation, we conclude that many aspects, such as projections, dynamical status, dynamical history, hydrostatic-equilibrium mass bias, temperature bias, environment, and the dependence of the biases on the mass of the systems, are contributing at the same time without a clear driving factor.

The most extreme points are mainly responsible for this feature. They are identifiable in Figure 7 by having either concentration above 9 or mass above $10^{15} h^{-1} M_{\odot}$. The points with high concentration register a large underestimate of the hydrostatic-equilibrium masses and the NFW masses, justified by a considerable temperature bias. Since this bias increases with the radius, it leads to high concentration values. On the other hand, the points with low concentration and high NFW mass are disturbed objects located in rich environments. They do not show major substructures, but their X-ray emission remains high up to the outskirts, causing a flattening of the mass profile. Note that the X-ray enhancement is present only in one of the three projections; therefore, there is no flattening of the intrinsic mass profile.

Finally, even excluding these points, the slope of c_x-M_x is more than 1σ larger than the intrinsic slope of c_i-M_i . The explanation is mostly related to two factors noticed above: restricting the external radial range produces an increase in the slope, and most massive systems go in both directions of reducing the concentration and increasing the mass and vice versa.

5. SELECTION FUNCTION

Selecting the sample according to the X-ray luminosity has been recognized as a source of bias in X-ray scaling relations (e.g., Nord et al. 2008; Pratt et al. 2009; Andreon et al. 2011; Andreon & Hurn 2012). Indeed, clusters in a specific X-ray luminosity bin correspond to a broad range of masses due to the wide scatter of the luminosity–mass relation (Pratt et al. 2009; Stanek et al. 2010; Mantz et al. 2010; Allen et al. 2011). The correspondence between the theoretical selection (based on mass) and the observational one (based on the X-ray emission) is, therefore, compromised. At the same time, also the c – M relation presents a significant dispersion: galactic or small group masses can have a concentration that varies even by an order of magnitude (e.g., Rudd et al. 2008; Ludlow et al. 2012; Bahé et al. 2012; De Boni et al. 2013).

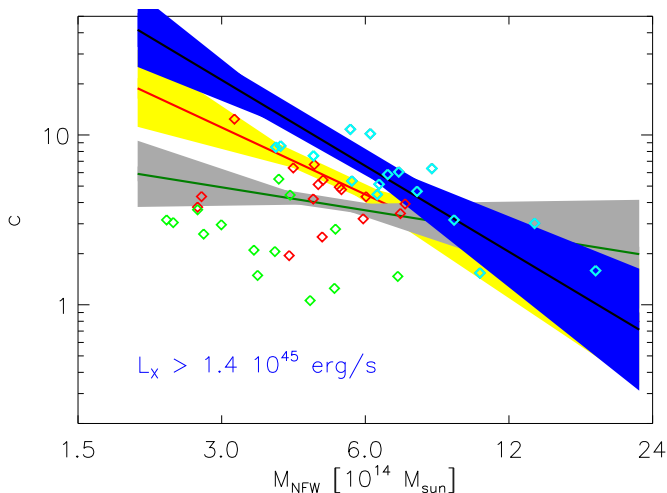


FIG. 10.— The concentration-mass relation for the synthetic X-ray catalogue. Clusters with [0.1-10] keV luminosity above 1.45×10^{45} erg/s are shown in cyan. The corresponding best-fitting relation is shown with a solid black line, while the blue region corresponds to the 1σ variation. The colors of the other symbols, lines, and regions are the same as in Figure 7.

Using our synthetic X-ray catalog, we investigate how the two scatters combine together when clusters are selected on the basis of their X-ray luminosity. In Figure 10, we plot our results where the blue shaded region is the c – M relation derived from clusters more luminous than 1.45×10^{45} erg s $^{-1}$ ⁹. The increase in slope and normalization with respect to the whole sample is quite clear: $\alpha = -1.68 \pm 0.55$, $c_0 = 8.93 \pm 2.07$, with an intrinsic scatter of about 12%. The statistics on which this analysis is based is quite limited, given the relatively small number of simulated clusters. In order to overcome this limitation and strengthen our conclusions, we also consider the set of clusters identified at $z = 0$ from a large cosmological box analyzed by De Boni et al. (2013), obtained for a *WMAP*–7 cosmology. The simulated volume of $(300h^{-1}\text{Mpc})^3$ was built with the Gadget-3 code evolving $(763)^3$ DM particles of mass $m \sim 3.7 \times 10^9 h^{-1} M_\odot$ and the same amount of gas particles. In Figure 11, we show the NFW concentrations and masses for ~ 400 relaxed objects taken from that sample. We select three mass bins ($1.5 < M_\odot/10^{14} < 2$, $2 < M_\odot/10^{14} < 2/7$, $M_\odot/10^{14} > 2.7$) to which we associate three soft-band X-ray luminosity bins obtained by adopting the luminosity–mass relation of the sample and using the X-ray [0.5–2] keV luminosity

⁹ The luminosity was computed in the [0.1-10] keV band.

ties provided by De Boni et al. (2011). The points associated with the three luminosity bins are shown with different colors. The horizontal solid red lines mark the median concentration of the luminosity bins while the median concentrations within the mass bins are shown with the black dashed lines. Quite clearly, the luminosity selection biases the concentration toward higher values in each bin, the effect being larger in smaller halos, thus inducing a steepening of the slope of the c – M relation.

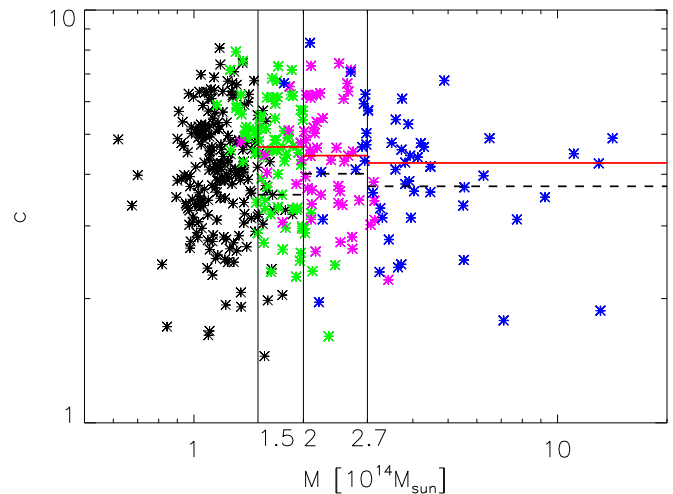


FIG. 11.— The concentrations and masses from the *WMAP* cosmological box of De Boni et al. (2013) at redshift zero. Three vertical lines show the boundaries of three mass bins to which we associate three soft-band ([0.5–2] keV) X-ray luminosity bins whose objects are colored in green, magenta, and blue from the least to the most luminous bin. Solid-red and dashed-black lines represent the median values of the concentrations obtained within the luminosity bins (points with the same color) and the mass bins (points within two vertical lines), respectively.

The findings derived from our synthetic catalog might explain the differences among the various observational c – M relations. While E10 and SA07, with a c – M slope around -0.4 , are based on very luminous clusters, the samples of B07 and Host & Hansen (2011), with slopes closer to the theoretical one, involve also early-type galaxies and small groups that *were not selected* for their X-ray power. The normalization spread among these works is also in agreement with our findings about the differences caused by the change of the radial range: SA07 limited the information to very central regions while all the other works extended beyond R_{2500} .

6. CONCLUSIONS

Recent claims about the discrepancy between the observed and simulated c – M relation were declared real. Here, we tested if the difference is instead induced by the two approaches followed to derive the values of NFW concentrations and masses. Specifically, we checked at the influence of (1) the radial range adopted to perform the NFW fit of the mass profile, (2) the baryonic-physics models included in the simulation, (3) the proper X-ray description, and (4) the impact of the selection function. To accomplish the first two tasks, we analyzed four sets of 52 clusters simulated four times, varying the description of the ICM physics and the synthetic catalog of 60 *Chandra*-like X-ray images (R12). The four sets of physics considered include dark matter (DM), no-radiative runs (NR), cooling, star formation and feedback by SN (CSF), and cooling, star formation,

and feedback from AGNs (AGN). The masses of the simulated clusters range from $\sim 1.5 \times 10^{14} M_{\odot}$ to $\sim 2.5 \times 10^{15} M_{\odot}$. This allows us to carry out a direct comparison with observational works that analyze massive clusters, and to extend previous theoretical studies on the $c-M$ relation that typically focused on the mass scale of galaxies and galaxy groups.

- *Radial range.* Using the DM set, we registered an increase in both slope and normalization of the $c-M$ relation when the most external radius considered during the NFW fit is reduced from outside the virial region ($2 \times R_{200}$) to the typical X-ray boundary ($0.6 \times R_{500} \sim 0.4 \times R_{200}$). Extending the fit to inner regions, instead, produces a higher normalization accompanied by a shallower slope. The opposite trend is found when we exclude the innermost regions from the fit of the mass profile, as done in weak-lensing studies. All these differences, even if robust (intermediate choices of either internal or external radius reproduce the same trend of changes in slopes and normalizations), are mild, $\Delta\alpha < 50\%$ and $\Delta c_0 < 10\%$. They, however, become more pronounced once baryons are introduced (α and c_0 increases up to 100% and 25%, respectively).
- *NFW fit and hydrodynamical simulations.* The total mass profiles of the radiative simulations (CSF and AGN) show large residuals in the innermost region. The cause is the efficient condensation of baryons in the form of a stellar component that drastically steepens the total density profile. The NR clusters at $z = 0$ are, instead, well described by the NFW formula. For all physics and radial ranges, the results related to the DM component are always robustly similar.
- *Baryon physics.* The relations derived from simulations with baryons have always a larger normalization than those from the DM halos. We confirm that adiabatic contraction is quite important in radiative simulations, a result that is in line with what was previously found in the analysis of less massive systems, although with a smaller amplitude (Rudd et al. 2008; Duffy et al. 2010). Studying the influence of the radial range on hydrodynamical simulations, we noticed that smaller objects are more affected by the change of either internal or external radius. The CSF set is characterized by a steeper and higher $c-M$ relation (increases around 30% in both normalization and slope with respect to the DM results in the SIM radial range). Both effects are strongly reduced when AGNs are included as a source of feedback. In this case, the slopes are much closer to the DM values, with variation of order of a few percent. The estimated differences for the NR data set are also less than 10%. Comparing the results of our intrinsic analysis with the observational ones, we found that the simulation slope overlaps with the values found only in Buote et al. (2007), whose sample, however, extends to lower-mass objects.
- *X-ray $c-M$.* While the change of the radial range and the baryonic physics contribute only partially to explain the gap between the theoretical and observed $c-M$ slope, the analysis performed on our synthetic X-ray catalog gave more insights. The hydrostatic-equilibrium assumption introduces a general reduction of the NFW masses

(25%) and an increase of the concentrations (20%). The first result is explained by the HE mass bias. Its radial dependence justifies the second finding. The NFW masses and concentration derived from the synthetic X-ray catalog have a huge dispersion (25% as intrinsic scatter) with respect to the intrinsic results (15% as intrinsic scatter). An increase in concentration corresponds to a decrease in mass and vice versa. The slope derived from our X-ray sample is not influenced by the construction of our sample. The relation steepening is caused by the concomitant presence of multiple effects such as projections, environment, dynamical state, dynamical history, mass bias, temperature bias, and their dependences on the radius and on the mass of the system. Our morphologically regular objects show a more than twice steeper slope with respect to the entire sample. This might seem in contrast with the finding of E10, who reported a shallower relation for their most relaxed systems. However, the selection of the two subsamples is based on different conditions: in our case regular systems have smaller third-order power ratio and centroid shift, while in E10 relaxed objects were defined as having lower central entropy level.

- *Selection function* Utilizing the data from a full cosmological box (the $(300h^{-1}\text{Mpc})^3$ volume simulated with a *wmap* cosmology at $z = 0$ of De Boni et al. 2013), we verify that selecting clusters via their X-ray luminosity biases the $c-M$ relation toward both a higher normalization and slope with respect to the mass-selected sample. We obtain, indeed, that more X-ray luminous clusters have, on average, higher concentration at fixed mass.

Numerical works present in the literature are based on many hundreds of halos. The effects of environment, dynamical status, and presence of substructures statistically cancel out when such a large set of objects is considered. This is not the case when few tens of objects are selected as done in observational works. The comparison between the two samples, therefore, cannot be as straightforward. From our analysis of the intrinsic profile, it emerged that smaller objects are more strongly affected by the choice of the radial range, and their mass profiles are more easily distorted by the mentioned effects. Furthermore, if groups or early-type ellipticals are chosen for their X-ray power, luckily, they will not represent the entire population of similar-mass objects, but will mostly be characterized by higher concentrations.

APPENDIX

In Table 3 we report the normalizations and slopes of the $c-M$ relations derived in the four sets of simulations at $z = 0.25$ adopting all the radial ranges presented above. The DM profiles within the hydrodynamical simulation behave very similarly to the profiles from the DM set; therefore, we choose to not list them. The significant radii R_{500} and R_{200} are recomputed at $z = 0.25$. Comparing the normalizations of the SIM radial range at $z = 0.25$ with those at $z = 0$, we notice that they are related to each other through: $c_0(z = 0) = c_0(z = 0.25) \times (1 + z)^{0.4}$.

Acknowledgment. We are grateful to the sharp and attentive report by the anonymous referee. E.R. thanks Cosimo Fedeli

TABLE 3

CONCENTRATION-MASS BEST-FIT PARAMETERS WITH 1σ ERROR OF THE HYDRODYNAMICAL SAMPLES AT REDSHIFT $z = 0.25$. FITTING RADIAL RANGES AND SYMBOLS AS IN TABLE 1. RESULTS OBTAINED FROM THE TOTAL DENSITY PROFILE.

		N	α	c_0	$\sigma_{\epsilon_{\log}}, \sigma_{\text{stat}}$
DM	SIM	43	-0.10 ± 0.04	3.42 ± 0.15	0.11, 0.03
	X-ray	43	-0.10 ± 0.04	3.43 ± 0.15	0.11, 0.04
	[0.06–0.4]	43	-0.17 ± 0.07	3.51 ± 0.20	0.10, 0.05
	[0.06–2.0]	43	-0.08 ± 0.04	3.47 ± 0.14	0.10, 0.02
	[0.03–1.27]	43	-0.08 ± 0.04	3.56 ± 0.15	0.11, 0.02
	[0.21–1.27]	43	-0.17 ± 0.11	3.10 ± 0.22	0.11, 0.06
NR	SIM	34	-0.07 ± 0.06	3.67 ± 0.16	0.11, 0.03
	X-ray	34	-0.07 ± 0.06	3.66 ± 0.16	0.10, 0.03
	[0.06–0.4]	34	-0.23 ± 0.16	3.71 ± 0.21	0.10, 0.05
	[0.06–2.0]	34	-0.05 ± 0.05	3.68 ± 0.15	0.10, 0.02
	[0.03–1.27]	32	-0.05 ± 0.05	3.64 ± 0.15	0.10, 0.02
	[0.21–1.27]	41	-0.03 ± 0.11	3.46 ± 0.22	0.11, 0.06
CSF	SIM	42	-0.18 ± 0.04	4.26 ± 0.19	0.11, 0.03
	X-ray	42	-0.18 ± 0.04	4.27 ± 0.20	0.11, 0.03
	[0.06–0.4]	42	-0.27 ± 0.04	4.85 ± 0.27	0.06, 0.04
	[0.06–2.0]	36	-0.14 ± 0.05	4.38 ± 0.20	0.11, 0.02
	[0.03–1.27]	–	–	–	–
	[0.21–1.27]	43	-0.21 ± 0.07	3.42 ± 0.21	0.11, 0.06
AGN	SIM	43	-0.09 ± 0.04	3.62 ± 0.16	0.11, 0.03
	X-ray	43	-0.10 ± 0.04	3.62 ± 0.16	0.11, 0.03
	[0.06–0.4]	43	-0.19 ± 0.06	3.81 ± 0.21	0.09, 0.04
	[0.06–2.0]	43	-0.09 ± 0.04	3.66 ± 0.15	0.10, 0.02
	[0.03–1.27]	41	-0.09 ± 0.04	3.94 ± 0.16	0.10, 0.02
	[0.21–1.27]	43	-0.14 ± 0.11	3.26 ± 0.21	0.11, 0.06

for sharing his results on the concentration–mass relation and for discussions at the early stage of this project and Cristiano De Boni for making available the tables of the *wmap* cosmological box of De Boni et al. (2011) and De Boni et al. (2013). We thank Volker Springel for providing us with the GADGET–3 code. Simulations have been carried out at the CINECA supercomputing centre in Bologna, with CPU time assigned through IS CRA proposals and through an agreement with University of Trieste. We acknowledge financial support by the following grants: National Science Foundation AST-1210973, SAO TM3-14008X (issued under NASA Contract No. NAS8-03060), ASI-INAF I/023/05/0 and I/088/06/0, Marie Curie Initial Training Network CosmoComp (PITN-GA-2009-238356) funded within the European Commission’s Framework Programme 7, PRIN-INAF09 project “Towards an Italian Network for Computational Cosmology”, PRIN-MIUR09 “Tracing the growth of structures in the Universe”, and INFN PD51. E.R. and M.M. would like to thank the Michigan Center for Theoretical Physics for supporting the collaboration.

REFERENCES

- Abadi, M. G., Navarro, J. F., Pardo, M., Babul, A., & Steinmetz, M. 2010, *MNRAS*, 407, 435
- Allen, S. W., Evrard, A. E., & Mantz, A. B. 2011, *ARA&A*, 49, 409
- Anders, E. & Grevesse, N. 1989, *Geochimica et Cosmochimica Acta*, 53, 197
- Andreon, S. & Hum, M. A. 2012, *ArXiv*: 1210.6232
- Andreon, S., Trinchieri, G., & Pizzolato, F. 2011, *MNRAS*, 412, 2391
- Bahé, Y. M., McCarthy, I. G., & King, L. J. 2012, *MNRAS*, 421, 1073
- Balaguera-Antolínez, A. & Porciani, C. 2013, *J. Cosmology Astropart. Phys.*, 4, 22
- Baldi, M. 2012, *Physics of the Dark Universe*, 1, 162
- Barnes, J. & White, S. D. M. 1984, *MNRAS*, 211, 753
- Battaglia, N., Bond, J. R., Pfommer, C., & Sievers, J. L. 2012, *ArXiv*: 1209.4082
- Bhattacharya, S., Habib, S., Heitmann, K., & Vikhlinin, A. 2013, *ApJ*, 766, 32
- Blumenthal, G. R., Faber, S. M., Flores, R., & Primack, J. R. 1986, *ApJ*, 301, 27
- Bonafede, A., Dolag, K., Stasyszyn, F., Murante, G., & Borgani, S. 2011, *MNRAS*, 418, 2234
- Borgani, S. & Kravtsov, A. 2011, *Advanced Science Letters*, 4, 204
- Bullock, J. S., Kolatt, T. S., Sigad, Y., Somerville, R. S., Kravtsov, A. V., Klypin, A. A., Primack, J. R., & Dekel, A. 2001, *MNRAS*, 321, 559
- Buote, D. A., Gastaldello, F., Humphrey, P. J., Zappacosta, L., Bullock, J. S., Brighenti, F., & Mathews, W. G. 2007, *ApJ*, 664, 123
- Chabrier, G. 2003, *PASP*, 115, 763
- Cui, W., Borgani, S., Dolag, K., Murante, G., & Tornatore, L. 2012, *MNRAS*, 423, 2279
- Dalal, N., Lithwick, Y., & Kuhlen, M. 2010, *ArXiv*: 1010.2539
- De Boni, C., Dolag, K., Ettori, S., Moscardini, L., Pettorino, V., & Baccigalupi, C. 2011, *MNRAS*, 415, 2758
- De Boni, C., Ettori, S., Dolag, K., & Moscardini, L. 2013, *MNRAS*, 428, 2921
- Dolag, K., Bartelmann, M., Perrotta, F., Baccigalupi, C., Moscardini, L., Meneghetti, M., & Tormen, G. 2004, *A&A*, 416, 853
- Dolag, K., Borgani, S., Murante, G., & Springel, V. 2009, *MNRAS*, 399, 497
- Duffy, A. R., Schaye, J., Kay, S. T., & Dalla Vecchia, C. 2008, *MNRAS*, 390, L64
- Duffy, A. R., Schaye, J., Kay, S. T., Dalla Vecchia, C., Battye, R. A., & Booth, C. M. 2010, *MNRAS*, 405, 2161
- Eke, V. R., Navarro, J. F., & Steinmetz, M. 2001, *ApJ*, 554, 114
- Ettori, S., Gastaldello, F., Leccardi, A., Molendi, S., Rossetti, M., Buote, D., & Meneghetti, M. 2010, *A&A*, 524, 68
- Fabjan, D., Borgani, S., Tornatore, L., Saro, A., Murante, G., & Dolag, K. 2010, *MNRAS*, 401, 1670
- Fedeli, C. 2012, *MNRAS*, 424, 1244
- Ferland, G. J., Korista, K. T., Verner, D. A., Ferguson, J. W., Kingdon, J. B., & Verner, E. M. 1998, *PASP*, 110, 761
- Gao, L., Navarro, J. F., Cole, S., Frenk, C. S., White, S. D. M., Springel, V., Jenkins, A., & Neto, A. F. 2008, *MNRAS*, 387, 536
- Gardini, A., Rasia, E., Mazzotta, P., Tormen, G., De Grandi, S., & Moscardini, L. 2004, *MNRAS*, 351, 505
- Gastaldello, F., Buote, D. A., Humphrey, P. J., Zappacosta, L., Bullock, J. S., Brighenti, F., & Mathews, W. G. 2007, *ApJ*, 669, 158

- Giocoli, C., Meneghetti, M., Ettori, S., & Moscardini, L. 2012, *MNRAS*, 426, 1558
- Gnedin, O. Y., Ceverino, D., Gnedin, N. Y., Klypin, A. A., Kravtsov, A. V., Levine, R., Nagai, D., & Yepes, G. 2011, *ArXiv*: 1108.5736
- Gnedin, O. Y., Kravtsov, A. V., Klypin, A. A., & Nagai, D. 2004, *ApJ*, 616, 16
- Governato, F., Zolotov, A., Pontzen, A., Christensen, C., Oh, S. H., Brooks, A. M., Quinn, T., Shen, S., & Wadsley, J. 2012, *MNRAS*, 422, 1231
- Grossi, M. & Springel, V. 2009, *MNRAS*, 394, 1559
- Gustafsson, M., Fairbairn, M., & Sommer-Larsen, J. 2006, *Physical Review D*, 74, 123522
- Haardt, F. & Madau, P. 2001, in *Clusters of Galaxies and the High Redshift Universe Observed in X-rays*, ed. D. M. Neumann & J. T. V. Tran
- Host, O. & Hansen, S. H. 2011, *ApJ*, 736, 52
- Hu, W. & Kravtsov, A. V. 2003, *ApJ*, 584, 702
- Humphrey, P. J., Buote, D. A., Brighenti, F., Flohic, H. M. L. G., Gastaldello, F., & Mathews, W. G. 2012, *ApJ*, 748, 11
- Kelly, B. C. 2007, *ApJ*, 665, 1489
- Khedekar, S., Churazov, E., Kravtsov, A., Zhuravleva, I., Lau, E. T., Nagai, D., & Sunyaev, R. 2013, *MNRAS*, 431, 954
- Killedar, M., Borgani, S., Meneghetti, M., Dolag, K., Fabjan, D., & Tornatore, L. 2012, *MNRAS*, 427, 533
- Komatsu, E., Smith, K. M., Dunkley, J., Bennett, C. L., Gold, B., Hinshaw, G., Jarosik, N., Larson, D., Nolte, M. R., Page, L., Spergel, D. N., Halpern, M., Hill, R. S., Kogut, A., Limon, M., Meyer, S. S., Odegard, N., Tucker, G. S., Weiland, J. L., Wollack, E., & Wright, E. L. 2011, *ApJS*, 192, 18
- Kravtsov, A. V. & Borgani, S. 2012, *ARA&A*, 50, 353
- Kwan, J., Bhattacharya, S., Heitmann, K., & Habib, S. 2012, *ArXiv*: 1210.1576
- Lau, E. T., Kravtsov, A. V., & Nagai, D. 2009, *ApJ*, 705, 1129
- Lau, E. T., Nagai, D., Kravtsov, A. V., & Zentner, A. R. 2011, *ApJ*, 734, 93
- Ludlow, A. D., Navarro, J. F., Li, M., Angulo, R. E., Boylan-Kolchin, M., & Bett, P. E. 2012, *MNRAS*, 427, 1322
- Macciò, A. V., Stinson, G., Brook, C. B., Wadsley, J., Couchman, H. M. P., Shen, S., Gibson, B. K., & Quinn, T. 2012, *ApJL*, 744, L9
- Mantz, A., Allen, S. W., Ebeling, H., Rapetti, D., & Drlica-Wagner, A. 2010, *MNRAS*, 406, 1773
- Martizzi, D., Teyssier, R., & Moore, B. 2012, *ArXiv e-prints*
- Meneghetti, M., Rasia, E., Merten, J., Bellagamba, F., Ettori, S., Mazzotta, P., Dolag, K., & Marri, S. 2010, *A&A*, 514, A93
- Navarro, J. F., Frenk, C. S., & White, S. D. M. 1996, *ApJ*, 462, 563
- Navarro, J. F., Frenk, C. S., & White, S. D. M. 1997, *ApJ*, 490, 493
- Neto, A. F., Gao, L., Bett, P., Cole, S., Navarro, J. F., Frenk, C. S., White, S. D. M., Springel, V., & Jenkins, A. 2007, *MNRAS*, 381, 1450
- Newman, A. B., Treu, T., Ellis, R. S., & Sand, D. J. 2013, *ApJ*, 765, 25
- Nord, B., Stanek, R., Rasia, E., & Evrard, A. E. 2008, *MNRAS*, 383, L10
- Ogrya, G. & Mori, M. 2011, *ApJL*, 736, L2
- Padovani, P. & Matteucci, F. 1993, *ApJ*, 416, 26
- Pedrosa, S., Tissera, P. B., & Scannapieco, C. 2009, *MNRAS*, 395, L57
- Piffaretti, R. & Valdarnini, R. 2008, *A&A*, 491, 71
- Pointecouteau, E., Arnaud, M., & Pratt, G. W. 2005, *A&A*, 435, 1
- Power, C., Navarro, J. F., Jenkins, A., Frenk, C. S., White, S. D. M., Springel, V., Stadel, J., & Quinn, T. 2003, *MNRAS*, 338, 14
- Pratt, G. W. & Arnaud, M. 2005, *A&A*, 429, 791
- Pratt, G. W., Croston, J. H., Arnaud, M., & Böhringer, H. 2009, *A&A*, 498, 361
- Ragone-Figueroa, C., Granato, G. L., & Abadi, M. G. 2012, *MNRAS*, 423, 3243
- Rasia, E., Ettori, S., Moscardini, L., Mazzotta, P., Borgani, S., Dolag, K., Tormen, G., Cheng, L. M., & Diaferio, A. 2006, *MNRAS*, 369, 2013
- Rasia, E., Mazzotta, P., Bourdin, H., Borgani, S., Tornatore, L., Ettori, S., Dolag, K., & Moscardini, L. 2008, *ApJ*, 674, 728
- Rasia, E., Meneghetti, M., & Ettori, S. 2013, *The Astronomical Review*, 8, 010000
- Rasia, E., Meneghetti, M., Martino, R., Borgani, S., Bonafede, A., Dolag, K., Ettori, S., Fabjan, D., Giocoli, C., Mazzotta, P., Merten, J., Radovich, M., & Tornatore, L. 2012, *New Journal of Physics*, 14, 055018
- Rasia, E., Tormen, G., & Moscardini, L. 2004, *MNRAS*, 351, 237
- Rudd, D. H., Zentner, A. R., & Kravtsov, A. V. 2008, *ApJ*, 672, 19
- Ryden, B. S. & Gunn, J. E. 1987, *ApJ*, 318, 15
- Schmidt, R. W. & Allen, S. W. 2007, *MNRAS*, 379, 209
- Sijacki, D., Springel, V., Di Matteo, T., & Hernquist, L. 2007, *MNRAS*, 380, 877
- Springel, V. 2005, *MNRAS*, 364, 1105
- Springel, V., Di Matteo, T., & Hernquist, L. 2005, *MNRAS*, 361, 776
- Springel, V. & Hernquist, L. 2003, *MNRAS*, 339, 289
- Stanek, R., Rasia, E., Evrard, A. E., Pearce, F., & Gazzola, L. 2010, *ApJ*, 715, 1508
- Stanek, R., Rudd, D., & Evrard, A. E. 2009, *MNRAS*, 394, L11
- Teyssier, R., Pontzen, A., Dubois, Y., & Read, J. I. 2013, *MNRAS*, 493
- Tissera, P. B., White, S. D. M., Pedrosa, S., & Scannapieco, C. 2010, *MNRAS*, 406, 922
- Tormen, G., Bouchet, F., & White, S. D. M. 1997, *MNRAS*, 286, 865
- Tornatore, L., Borgani, S., Dolag, K., & Matteucci, F. 2007, *MNRAS*, 382, 1050
- van Daalen, M. P., Schaye, J., Booth, C. M., & Dalla Vecchia, C. 2011, *MNRAS*, 415, 3649
- Vikhlinin, A., Burenin, R. A., Ebeling, H., Forman, W. R., Hornstrup, A., Jones, C., Kravtsov, A. V., Murray, S. S., Nagai, D., Quintana, H., & Voevodkin, A. 2009, *ApJ*, 692, 1033
- Vikhlinin, A., Kravtsov, A., Forman, W., Jones, C., Markevitch, M., Murray, S. S., & Van Speybroeck, L. 2006, *ApJ*, 640, 691
- Voit, G. M. 2005, *Reviews of Modern Physics*, 77, 207
- Walker, S. A., Fabian, A. C., Sanders, J. S., Simionescu, A., & Tawara, Y. 2013, *MNRAS*, 432, 554
- Wiersma, R. P. C., Schaye, J., & Smith, B. D. 2009, *MNRAS*, 393, 99
- Zemp, M., Gnedin, O. Y., Gnedin, N. Y., & Kravtsov, A. V. 2012, *ApJ*, 748, 54
- Zhao, D. H., Jing, Y. P., Mo, H. J., & Börner, G. 2009, *ApJ*, 707, 354
- Zhu, X.-J. & Pan, J. 2012, *Research in Astronomy and Astrophysics*, 12, 2